



Contents lists available at ScienceDirect

# International Journal of Applied Earth Observations and Geoinformation

journal homepage: [www.elsevier.com/locate/jag](http://www.elsevier.com/locate/jag)

## Land subsidence modeling and assessment in the West Pearl River Delta from combined InSAR time series, land use and geological data

Ziyue Liu<sup>a</sup>, Alex Hay-Man Ng<sup>a,b,\*</sup>, Hua Wang<sup>a</sup>, Jiawei Chen<sup>a</sup>, Zheyuan Du<sup>c,d</sup>, Linlin Ge<sup>d</sup><sup>a</sup> Department of Surveying Engineering, Guangdong University of Technology, Guangzhou, China<sup>b</sup> Key Laboratory for City Cluster Environmental Safety and Green Development of the Ministry of Education, Guangdong University of Technology, Guangzhou, China<sup>c</sup> Geoscience Australia, Canberra, Australia<sup>d</sup> School of Civil and Environmental Engineering, University of New South Wales (UNSW), Sydney, NSW 2052, Australia

## ARTICLE INFO

## Keywords:

Land subsidence  
Time-series SAR Interferometry  
InSAR  
Land-use  
the West Pearl River Delta

## ABSTRACT

West Pearl River Delta (WPRD) is sinking as a result of the jointed effect of natural and anthropogenic factors. Land subsidence has increasingly become a concern because of tremendous population growth and rapid urbanization over this region in the last few decades. In this study, sixty-seven Sentinel-1 images, acquired between 2016 and 2021, were analyzed with the persistent scatterer interferometry technique (PSI), to monitor and reveal the ground subsidence characteristics in the WPRD. It is found that the overall vertical deformation velocities observed in the WPRD ranged between  $-70$  mm/year and  $10$  mm/year. Three subsidence bowls were found in the study area (Gaolan island of Zhuhai, the junction area of Zhuhai and Zhongshan, and the junction area of Zhongshan and Jiangmen). The spatial-temporal subsidence characteristics have been analyzed. It is discovered that the ground subsidence is mostly dispersed in Quaternary deposits and is highly relevant to the thickness of sediments, indicating that soft soil consolidation is one of the primary causes contributing to land subsidence. Furthermore, land use maps for 2016 and 2021 were generated using Landsat-8 images for the investigation on the relationship between land subsidence and land use. The results obtained from analysis demonstrated that the rapid subsiding areas mainly occurred in the land-use classes as follows: aquaculture, urban land, and agricultural land. The land use conversion pattern with more significant anthropogenic influence usually causes a higher subsidence rate. In addition, based on soft soil thickness, groundwater exploitation, land use, elevation, and strata lithology, a Random Forest Regression (RFR) model was used to predict subsidence rates ( $R^2 = 0.631$ ,  $RMSE = 2.7$  mm/year). The importance of these influencing factors of land subsidence was calculated based on the RFR algorithm. The results indicated that soft soil thickness, elevation, groundwater exploitation, strata lithology, and landcover type are the most significant factors affecting subsidence. The applicability of geological data and land-use history for land subsidence prediction has been demonstrated with the use of the RFR algorithm.

### 1. Introduction

Ground subsidence is a very serious issue in coastal areas where several river deltas across the world are vulnerable to it. (Galloway et al., 2016). Continuous subsidence can also aggravate the risks of coastline erosion, flooding (Zhu et al., 2020), tidal inundation or wetlands loss, and sea-level rise, causing substantial economic loss and threat to lives (Chen et al., 2012). Therefore, continuous monitoring and analysis of ground subsidence are crucial for assessing the risk and ensuring the sustainable and stable development of coastal delta regions.

The traditional geodetic methods for monitoring ground deformation, e.g. Global Navigation Satellite System (GNSS) and leveling, are constrained by their poor spatial coverage and resolution. Interferometric Synthetic Aperture Radar (InSAR) provides a range of substantial advantages for high spatial resolution and regional scale deformation measurements. InSAR has already demonstrated its capability for monitoring land deformation in various applications, for example, urban subsidence monitoring (Du et al., 2021; Wang et al., 2012), volcanic and earthquake studies (Wang et al., 2019a), groundwater exploitation (Bakr, 2015), slope stability monitoring (Kuang et al., 2022) and subsidence induced by mining activities (Yang et al., 2016).

\* Corresponding author.

E-mail addresses: [hayman.ng@gdut.edu.cn](mailto:hayman.ng@gdut.edu.cn), [hayman.ng@gmail.com](mailto:hayman.ng@gmail.com) (A.H.-M. Ng).<https://doi.org/10.1016/j.jag.2023.103228>

Received 24 August 2022; Received in revised form 6 February 2023; Accepted 8 February 2023

Available online 18 February 2023

1569-8432/© 2023 The Authors. Published by Elsevier B.V. This is an open access article under the CC BY-NC-ND license (<http://creativecommons.org/licenses/by-nc-nd/4.0/>).

Pearl River Delta (PRD), one of China's most dynamic and urbanized regions, has the greatest urban agglomerations in the world with approximately 70 million in population, and exceeding 10 trillion RMB (about \$1.47 trillion) in the gross domestic product (GDP). Since 1850, the PRD has obtained 1160 km<sup>2</sup> of new land. During this period, the PRD has undergone intensive anthropogenic activities, including infrastructure construction, groundwater withdrawal, and land reclamation. The southern part of PRD is in low-lying land where the geological environment is fragile due to the mutual influence of oceans and land. The dense river network, abundant aquaculture and anthropogenic activities (e.g. groundwater extraction and land reclamation) in this area can generate varying degrees of subsidence. In addition, most of these regions are located at or below sea level (see the white area in Fig. 1a), and the joint effect of sea level rise and ground subsidence can further intensify the risk of coastal inundation. Therefore, it is necessary to analyze land subsidence in the PRD systematically to reduce the probability of a subsidence disaster.

InSAR has already been applied for investigating the land deformation phenomenon at PRD as reported in a number of previous studies, including Wang et al. (2012), Xu et al. (2016), Ng et al. (2018), Ma et al. (2019), Du et al. (2020), Li et al. (2020), etc. These studies have been conducted on various places in PRD using SAR data acquired by different satellites. Their results suggest that the land subsidence in PRD is related to soft soil layer compaction, urban development, land reclamation, subway construction, geological settings, and land use (aquaculture and agricultural areas).

In this paper, the land deformation in the West PRD (WPRD) is investigated using Time-series InSAR (TS-InSAR) analysis. A summary of relevant InSAR studies for WPRD can be found in Table 1. Recent land subsidence studies have suggested that land subsidence could show a relevant response to the change in land-use (Minderhoud et al., 2018; Umarhadi et al., 2022). The effect of different land cover types and land-use change on the land subsidence, especially for the WPRD, has been rarely studied but is of great interest in the understanding of the subsidence phenomenon. More importantly, there are few studies on the quantitative analysis of the significance of multiple contributing factors to land subsidence. As a result, it is necessary to further analyze the importance of each subsidence related influencing factor to determine all effective contributing factors for WPRD. In this work, the PSI technique has been carried out to investigate the land deformation in the WPRD with 67C-band Sentinel-1A (S1) images from 2016 to 2021. The combination of InSAR and optical remote sensing technology was then used to investigate the features of land deformation in the various land-use types and land-use change in the WPRD. Natural factors and

**Table 1**

Summary of relevant studies using InSAR technologies over West PRD (WPRD).

Reference	Location	Method	SAR data	Key results/main causes of subsidence
(Chen et al., 2012)	Greater Pearl River Delta	Improved PSI	ENVISAT C-band	Urban expansion; reclamation; the distribution of river and Quaternary sediments
(Ma et al., 2019)	Guangdong–Hong Kong–Macao Greater Bay Area	MT-InSAR	Sentinel-1C-band	Quaternary sediment consolidation; Groundwater extraction; artificial loading
(Du et al., 2020)	Coastal Areas of Guangdong	SBAS InSAR and TCP InSAR	PALSAR L-band	Quaternary sediment thickness; aquaculture areas
(Li et al., 2020)	Pearl River Delta	SBAS InSAR	PALSAR L-band	The thickness of soft soils; geological evolution; reclamation; pumping groundwater for aquaculture

anthropogenic activities of the study area have also been assessed to examine the impacts on land subsidence. Finally, according to the main land subsidence factors, a land subsidence prediction model is established by using the Random Forest Regression (RFR) approach, and the importance of each factor is evaluated.

## 2. Study area and datasets

### 2.1. Geological background

The WPRD is located at the West Bank of the Pearl River in Guangdong Province, including the Zhuhai-Zhongshan-Jiangmen (ZZJ) economic circle (Fig. 1a). The study area has a superior geographical location, which is adjacent to Macau on the south, connected to Guangzhou and Foshan area on the north, and to Hong Kong on the east. In the WPRD, Zhuhai city has the greatest marine area (about 6,000

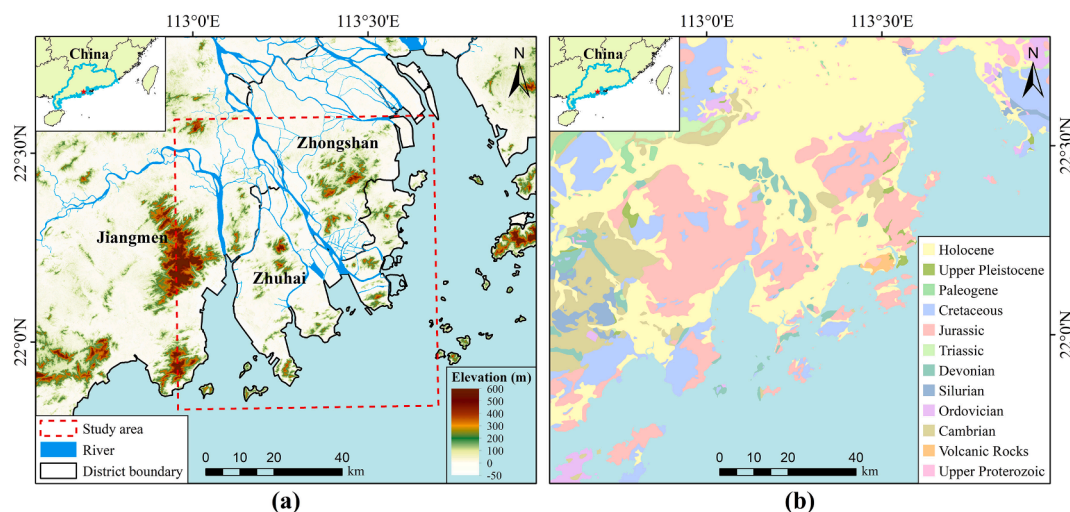


**Fig. 1.** (a) Location of WPRD (red star at the upper left sub-figure). The red dotted box and black lines represent the study area and district boundary, respectively; (b) the strata lithology in the WPRD. (For interpretation of the references to colour in this figure legend, the reader is referred to the web version of this article.)

km<sup>2</sup>), the most islands (about 150), and the longest coastline (about 600 km). The terrain of this region is quite flat with an elevation below 50 m in most of the region (Fig. 1a). Because of the effect of subtropical monsoon climate, WPRD usually receives abundant rainfall from April to September, with an average annual rainfall varying from 1600 to 2000 mm. During this period, the study area often suffers from typhoons and floods.

The Geologic setting map of WPRD (Fig. 1b) shows that the Quaternary sediments are the dominant geological structure, with the thickness varying from 10 m to over 40 m. Quaternary is the latest period of the Cenozoic, including the Pleistocene and Holocene. In the PRD plain, soft soil is mainly three transgressive periods of sediments from Upper Pleistocene to Holocene (32000 to 22000 years ago, 7500 to 5000 years ago, and 2500 years ago, respectively). According to the formation time, origin, and engineering geological properties, the soft soil can be divided into three layers with other non-transgressive deposits: the third, the second, and the first soft soil layer from bottom to top (Wang et al., 2019b). Three soft soil layers are generally distributed in the southern part of the Panyu district in Guangzhou, the southeast part of Foshan, the eastern part of Jiangmen, and the northern part of Zhongshan city. At the same time, other regions mainly develop the first and second soft soil layers (Lu, 2006).

## 2.2. Datasets

Sixty-seven ascending S1 images acquired from 5 January 2016 to 13 July 2021 were used in this study. The average incidence angle for all these S1 images, which were acquired in ascending orbit, is 39.5° (Track 011). The imaging mode is the Interferometric Wide Swath (IW) mode, and the polarization mode is VV. The 1-arc second Shuttle Radar Topography Mission (SRTM) DEM data (Rabus et al., 2003) was used to remove the topographic phase from InSAR signals. The reference image was selected as the one collected on September 15th, 2018. Fig. 2 shows the distribution of the perpendicular and temporal baselines of 66 interferometric pairs. In addition to the SAR datasets, the land-use classification maps for 2016 and 2021 were generated using median composited from all the Landsat-8 surface reflectance images in 2016 (28 images) and 2021 (31 images) via Google Earth Engine (GEE) cloud-based platform.

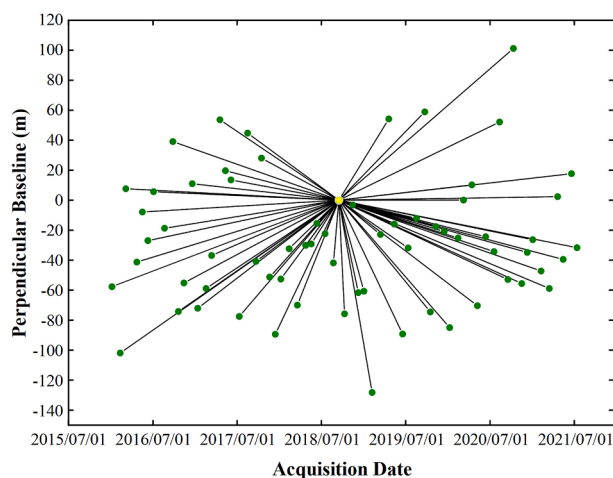


Fig. 2. Temporal and perpendicular baseline distribution of S1 dataset. The yellow dot represents the reference image. (For interpretation of the references to colour in this figure legend, the reader is referred to the web version of this article.)

## 3. Methodology

### 3.1. Time-series InSAR (TS-InSAR) analysis

TS-InSAR technique was conducted to measure the land subsidence in the WPRD with S1 images. The differential interferograms stacks were generated using the InSAR Scientific Computing Environment (ISCE) software (Rosen et al., 2012). Then GEOS-PSI, an in-house developed persistent scatterer interferometry (PSI) analysis software, was performed to study the land deformation evolution at WPRD (Ng et al., 2012a; Ng et al., 2012b). The basic procedures for the PSI analysis used in this work were as follows. Firstly, the Persistent Scatterers candidates (PSC) were selected based on the amplitude dispersion index (ADI), and all pixels with  $ADI < 0.4$  were selected (Ferretti et al., 2001). An initial reference network was generated using triangulation network for PSC with  $ADI < 0.25$ . The least-squares ambiguity decorrelation approach (LAMBDA) was used to compute the model parameters at each arc of the reference network. Then, the reliability of the estimated model parameters was assessed by the ensemble phase coherence (Ferretti et al., 2001). The ensemble phase coherence threshold of 0.6 was used because of the availability of large image stack (Colesanti et al., 2003). Spatial integration was subsequently conducted using robust fitting. The PS candidates, that are not selected for the construction of the reference network, were included into the network using the adaptive estimation strategy (Ng et al., 2012b). The spatial-temporal filtering approach was utilized to correct the atmospheric and orbital errors. The unmodeled deformation components were then extracted from the unwrapped residual phase. Finally, the time-series deformation results were derived by joining the linear deformation (modeled) and the non-linear deformation (unmodeled). The details of the TS-InSAR processing flow are described in the Supplementary section (see supplementary S1.1).

The displacement time series in the WPRD are measured along the radar's line of sight (LOS) direction. Since only the ascending images were available, it is assumed that the majority of deformation in the WPRD, especially in the coastal area, is in the vertical direction (Du et al., 2020). Hence, the horizontal displacement is ignored here, and the deformation measured in the LOS direction is thus directly projected to the vertical direction.

### 3.2. Land-use classification

The Random Forest Classifier (RF) (Breiman, 2001), a supervised machine learning algorithm widely used in classification problems, was applied to generate the land-use classification maps using the GEE platform. The CFMASK algorithm (Foga et al., 2017) was used for pre-processing and to mask the cloud for the Landsat-8 SR data. The median composite method was then used to generate the cloud-free composite images of the study area. The spectral features, i.e., Red, Green, Blue, NIR, SWIR1, and SWIR2 bands were selected as the input feature variables. Spectral indexes including the NDVI, the NDBI, and the NDMI were computed and included in the data classification processing to enhance the discrimination of various land-use types. The reference data were collected by visual interpretation from Google Earth, and the samples were randomly selected over the study area. A total of 675 samples for each Landsat image were chosen for all classes and were randomly split into 2 parts: 70 % and 30 % for training dataset and validation dataset, respectively. The training data was used for training a random forest with 100 decision trees. A total of 7 land classes were formed: urban, agriculture, aquaculture, forest, water, bare land, and mangroves. The procedure was repeated to generate two consistent land-use maps 2016 and 2021. Finally, the raster image was exported to vector format for superposition analysis with InSAR results.

### 3.3. Land subsidence modeling

According to the InSAR results, the influencing factors of subsidence

were determined by combining regional topographic and geological characteristics and served as the independent variables, including the thickness of soft soil, groundwater exploitation, land-use history data (1980, 1995, 2000, 2005, 2010, 2015, 2018, 2016, 2020 and 2021), elevation and strata lithology. The subsidence rate of PS points in this study was used as the dependent variable. In addition to the generated land use for 2016 and 2021 in this study, other land-use history data were obtained from the Chinese Academy of Sciences with a spatial resolution of 30 m (Xu et al., 2018). The elevation data was acquired from the SRTM DEM. These factors and InSAR-derived subsidence rates were imported into the GIS system to establish the database. A total of 1,749,141 samples were divided: 70 % of samples for training and the remaining 30 % for validation. In this study, the number of trees was set to 1000 based on Grid Search with Cross Validation. The learning performance was assessed using 10-fold cross-validation and the accuracy of the model was quantitatively evaluated by calculating the root mean square error (RMSE) of the validation dataset (Umarhadi et al., 2022). In order to assess the significance of each input variable to the subsidence model, the importance of each influence factor was calculated based on Gini importance (mean decrease impurity) (Louppe et al., 2013). The data processing workflow used in this study is shown in Fig. 3. See Supplementary S1.2 for detailed information of the land subsidence model construction.

### 4. Results

#### 4.1. InSAR results

A subsidence rate map in the WPRD generated from the S1 images between 2016 and 2021 is shown in Fig. 4a. An average subsidence velocity of 0.2 mm/year and the standard deviation of 2.8 mm/year are obtained (Fig. 4b). The PS points with subsidence rates ranging from 10 to -10, -10 to -30, and -30 to -50 mm/year take account for 95.6 %, 3.8 %, and 0.5 % of all PS points, respectively.

The results show that most parts of the study areas remain stable. Three subsidence bowls were found in the study region (see Fig. 4a): (1) the junction of Zhuhai and Zhongshan, with an average subsidence rate of -16 mm/year; (2) the junction of Jiangmen and Zhongshan, with a rate of about -13 mm/year; (3) the Gaolan island of Zhuhai, the most severe settlement in the reclamation regions (in areas between the 1979 and 2020 coastlines marked in Fig. 4a), and the peak settlement rate

observed here is -87.3 mm/year. In addition, small-scale subsidence was also found in some areas, for example, the Xiangzhou district of Zhuhai (Fig. 4a). Three points (P1, P2, P3) were selected to study their deformation time series (see Fig. 4c). It is found that the linear displacement occurs at the three points.

#### 4.2. InSAR accuracy assessment

To evaluate the accuracy of the subsidence results, the leveling benchmarks acquired in 2019 from Li et al. (2021) were collected. These benchmarks were in three main subsidence regions in Zhuhai. Fig. 5 depicts the locations of these leveling points. Since the PS pixels and leveling benchmarks are not located exactly same place, it is necessary to minimize the effect of the geolocation errors between the two datasets such that the two techniques are comparable. The buffer zones of 60 m were established for each leveling benchmark, all PS pixels within the same buffer were collected and the deformation value was obtained by averaging the deformation value at these PS pixels (Table 2). The maximum absolute difference obtained is approximately 4.7 mm/year. To further verify the PSI results, a field survey is conducted in the WPRD, including P1, P2 and P3. P1 is located in the reclamation area. Most of the nearby areas are paddy fields and aquaculture ponds, so the subsidence is most likely caused by groundwater extraction for crop irrigation and aquatic products. P3 is located in Da'ao town in Jiangmen, where wall cracking has occurred in many rural residential areas due to land subsidence. The field survey suggests that the location with cracks on infrastructures found agrees well with the subsidence regions from the InSAR result (Fig. 6).

#### 4.3. Land-use classification and change analysis

Fig. 7 shows the Landsat-8 derived land cover classification maps in 2016 and 2021. The overall accuracies of classification maps based on the confusion matrix are 92.8 % and 91.3 %, respectively. The land-use transition matrix during this period is shown in Table S1. The findings indicate that some changes have taken place in the land-use patterns between 2016 and 2020. Referring to the land-use transition matrix, it is found that the most significant change occurred in the expansion of urbanized areas, reflecting the growing population and urbanization of the WPRD. The area of urban land has increased by 166.44 km<sup>2</sup>, and the predominant origin of the increase is agricultural land. The main pattern

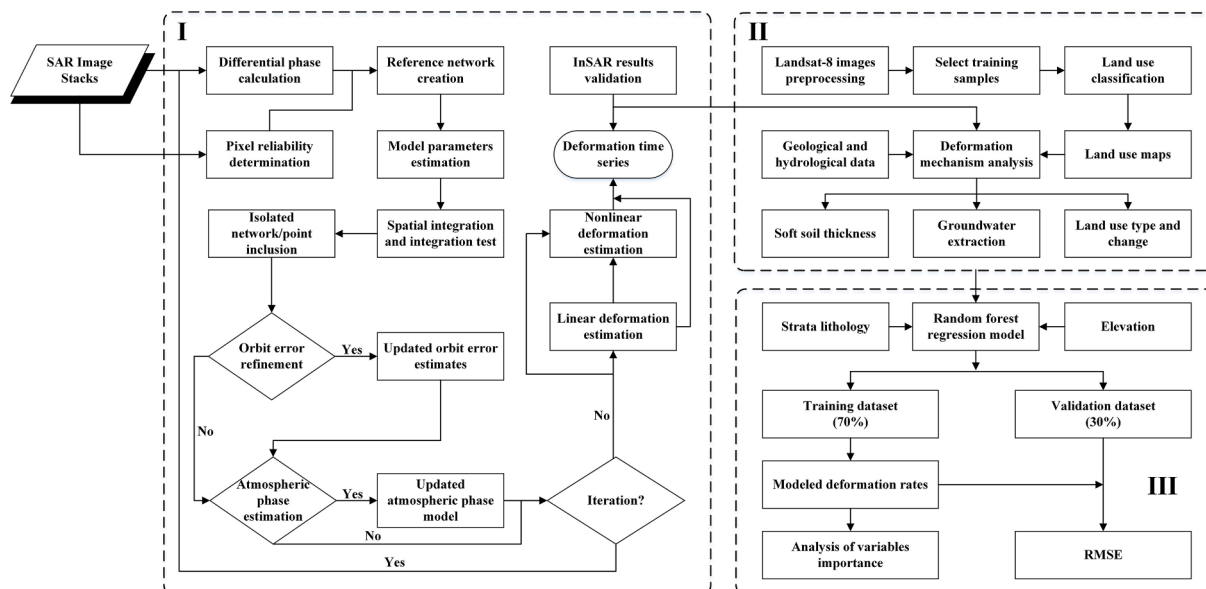
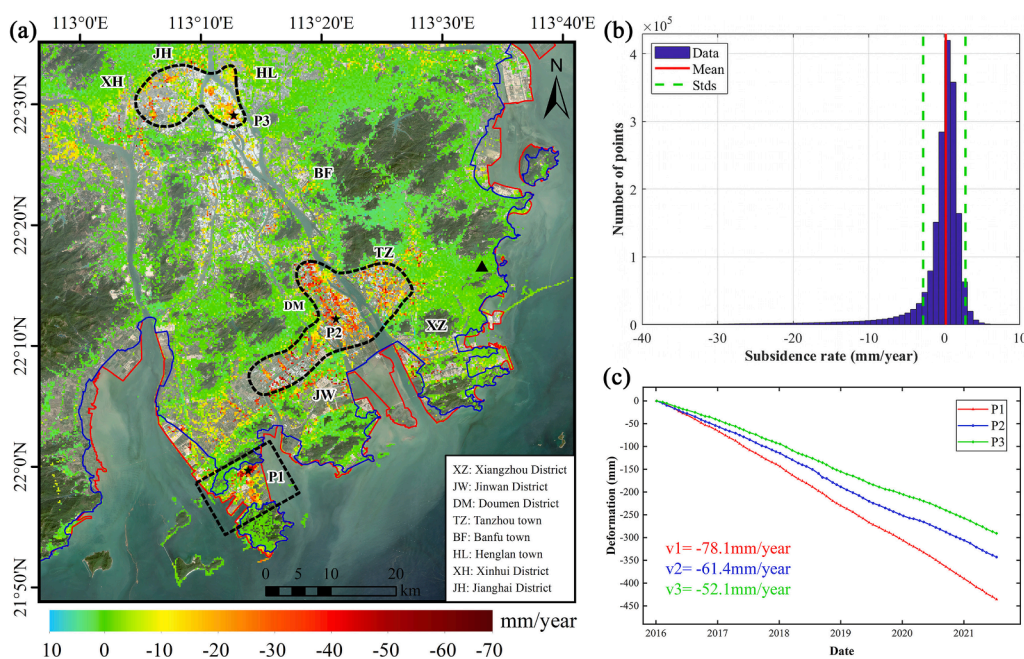


Fig. 3. Data processing workflow.



**Fig. 4.** (a) Subsidence rate map of the WPRD overlaid on the Sentinel-2 optical image. Black dotted polygons represent the three primary subsidence bowls. The black triangle indicates the position of the reference point. Blue and red lines indicate the coastal lines in 1979 and 2020, respectively. P1, P2, and P3 are the three points in the corresponding subsidence bowls that are chosen for time-series analysis; (b) histogram plot of subsidence rate; (c) InSAR-measured subsidence time-series at P1, P2, and P3 in Fig. 4a. (For interpretation of the references to colour in this figure legend, the reader is referred to the web version of this article.)

of transformation of barren land was mostly converted into urbanized and agricultural land. The area of agricultural and forest land has decreased by 64.72 km<sup>2</sup> and 51.03 km<sup>2</sup> respectively. Table S1 shows a reduction in the area of aquaculture, mainly converted to urban and agricultural areas. Moreover, it is noteworthy that the area of mangrove wetlands has increased slightly, and the mangroves are mainly distributed on Qi'ao Island in Zhuhai city (Fig. 7).

#### 4.4. Subsidence model estimation

Based on the above-selected input feature parameters, the subsidence model was established (Fig. 8). A good agreement between the modeled subsidence rates and the InSAR results has been observed with similar spatial patterns. All three subsidence bowls have been observed from the modeled subsidence. The RMSE between the InSAR observations and predicted subsidence rates is 2.7 mm/year calculated from validation samples ( $R^2 = 0.631$ ) and their absolute difference ranges from 0 to 5 mm/year, which accounted for 94.6 % of the validation samples. The importance of each variable is calculated as shown in Fig. 9. Three most significant causes of land subsidence, in order of decreasing significance, were found using the RFR algorithm to be the thickness of soft soil, elevation, groundwater exploitation, and strata lithology, followed by different land-use types. Aquaculture, urban land, and agriculture are the most significant land-use related factors affecting subsidence. Bare land and forest areas were the less important land-use related factors, where the influence from the rest of the land-use types is almost neglectable.

## 5. Discussion

### 5.1. Comparison of subsidence rates between 2006 and 2021

A comparison between the deformation measurements obtained in this and previous works has been conducted. In general, the magnitudes and patterns of deformation between 2016 and 2021 obtained in this work agree with the historical deformation patterns from previous studies, i.e., between 2006 and 2011 (Chen et al., 2012; Du et al., 2020; Li et al., 2020), and between 2015 and 2017 (Ma et al., 2019). It can be clearly observed that continuous subsidence occurred in the PRD from 2006 to 2021. The three large subsidence bowls have been found in all

the locations in these studies. However, there are slight differences in the magnitude of deformation observed. Both Du et al. (2020) and Ma et al. (2019) suggested that the maximum subsidence rate occurred in the reclamation area located in Zhuhai (P1), which is consistent with this study. But compared to the peak subsidence rates from these studies (-112.3 mm/year and -150.9 mm/year), slightly lower subsidence rate has been observed in this work (-87.3 mm/year). There are three possible reasons that can cause the inconsistency in the peak subsidence rate observed: (1) higher average coherence is expected with a relatively short time and hence more measurement points were detected in Ma et al. (2019); (2) ALOS-1 PALSAR data have a longer wavelength to identify greater subsidence in Du et al. (2020); (3) the settlement has been decreasing gradually due to a longer time for the consolidation of reclamation materials. Li et al. (2020) suggested that the most serious subsidence was found in the junction of Jiangmen and Zhongshan (P3), but this subsidence rate (<-70 mm/year) is much lower than the subsidence rate at the reclamation area in Zhuhai (P1) according to Du et al. (2020), Ma et al. (2019), and this study. This suggests that the subsidence in settlement bowls corresponding to P1 should be the most significant amongst the three, which is consistent with this study. In addition, Chen et al. (2012), Du et al. (2020), and Li et al. (2020) demonstrated that the junction of Zhongshan and Jiangmen (P3) experienced larger land subsidence than the junction of Zhuhai and Zhongshan (P2), which is contrary to the results of Ma et al. (2019) and this study. This could indicate that the land subsidence in the junction of Jiangmen and Zhongshan probably has a trend of mitigation (2006 ~ 2011 to 2016 ~ 2021).

### 5.2. The relationship between land subsidence and the soft soil thickness

The soft soil map of WPRD is shown in Fig. 10b, with the borehole-derived soft deposit thickness data provided by Lai et al. (2021) and Lu (2006). The soft soil is mostly found near the river and in coastal regions. As can be observed, there are six categories for the thickness of soft soil: 0–5 m, 5–10 m, 10–20 m, 20–30 m, and > 40 m. The thickness of soft soil varies in different regions, which is thin when close to the mountain, but thick when close to the river and seas (see Fig. 10b). The soft soil layers are mainly composed of clayey soil, muck, and muck soil, which are notable for their high water content, strong compressibility, and poor shear strength (Lu, 2006). Therefore, the self-consolidation and

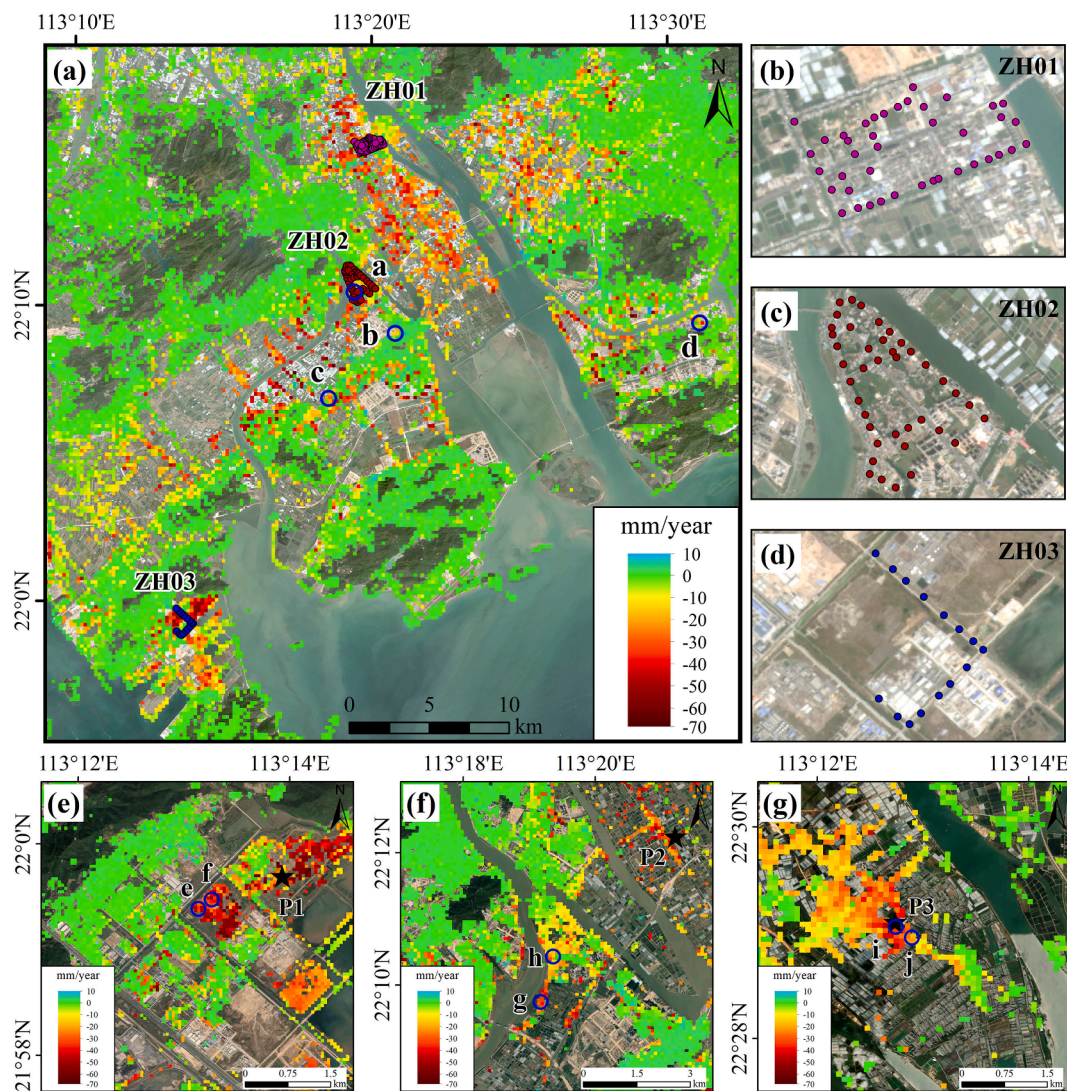


**Fig. 5.** (a) The leveling benchmarks of the three main subsidence areas in Zhuhai. The blue circles (a, b, c, and d) are the locations of the field investigation areas correspondingly shown in Fig. 6 (a-d); (b-d) the locally enlarged view and corresponding optical images of the leveling benchmarks in (a); (e-g) the subsidence rate maps near P1, P2, and P3, and the blue circles (e, f, g, h, i, and j) are the locations of the field investigation areas correspondingly shown in Fig. 6 (e-j). (For interpretation of the references to colour in this figure legend, the reader is referred to the web version of this article.)

**Table 2**  
Comparison of average subsidence rate between PSI- and leveling-measurements.

Benchmark Identifier	Mean subsidence rate (mm/year)		
	Leveling	PS	Absolute difference
ZH01	-8.8	-9.4	0.6
ZH02	-13.9	-10.8	3.1
ZH03	-14.2	-18.9	4.7

compaction of soft soil and the long-lasting buildings and infrastructure loading can cause land subsidence.

To analyze the influence of soft soil thickness to subsidence, a quantitative analysis has been conducted to investigate the connection between land subsidence and soft soil thickness. The histogram of the subsidence rates at different soft layer thicknesses was calculated. The results are shown in Fig. 10d. It is found that subsidence is mostly localized in the soft soil layers, and severe subsidence (<-20 mm/year) mainly occurred in areas with soft soil thickness >40 m. Additionally, a superimposed analysis of the different thicknesses of soft soil and land subsidence is conducted (Table 3). Correlation between subsidence rate

and soft soil thickness has been observed. The association between subsidence rate and soft layer thickness for various land-use types was thus investigated using statistical regression analysis (see Fig. 10e). The number at the end of each interval of soft layer thickness (i.e., 5, 10, 20, 30, 40, and 50 m) was selected to evaluate the correlation. A quadratic polynomial expression was established through the comparison of the linear and nonlinear relationship between them. Based on least-squares estimation, the regression coefficients at different land-use classes were calculated and evaluated by a hypothesis test. The determination coefficient R square (95 % confidence level) was employed to estimate the goodness of fit (Fig. 10e). The results suggest that land displacement is highly related to the distribution of soft soil in the WPRD and greater soft soil thickness leads to larger subsidence rates.

### 5.3. The relationship between groundwater exploitation and subsidence

According to the geological survey (Wang et al., 2019b; Zhang, 1997), there are two main types of groundwater systems in the WPRD: fractured bedrock aquifers and loose rock pore aquifers. Fractured bedrock aquifer is mainly distributed in mountainous areas with poor water resources. Except for a small area of layered rock fissure water



**Fig. 6.** The field investigation photos in Zhuhai. (a-b) Wall cracking phenomenon caused by foundation subsidence in Doumen district; (c-d) pavement cracking phenomenon caused by subgrade subsidence in Jinwan and Xiangzhou districts; (e-f) the reclamation areas near P1; (g-h) the nearby areas of P2; (i-j) the nearby areas of P3.

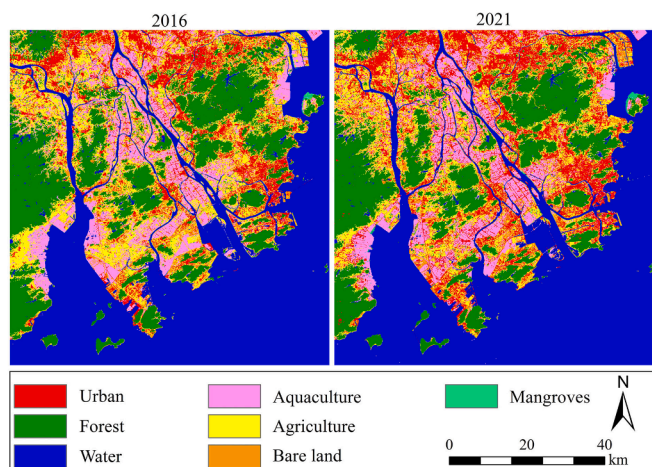


**Fig. 7.** The land-use classification map in the study area derived from Landsat-8 images of 2016 and 2021.

whose lithology is sandstone and siltstone in the southern part of the study area, the rest are block rock fissure water composed of biotite granite. While loose rock pore aquifers are mainly distributed along rivers, mountain valleys, and coastal plains, the aquifer is feeble confined water and consists of sand, gravel clay, and silty clay, with moderate water resources. Groundwater in the study area is mainly saltwater and brackish water, and the supply of freshwater is mainly derived from surface water. The aquifers are shallow with the depth of the water table (old stone well) between 3 and 10 m in general. The depth of pumping wells is mainly 20–35 m in Zhuhai and 10–20 m in Zhongshan, but there are a small number of wells with a depth varied from 40 m to 50 m in Zhuhai (Wang et al., 2019b).

Groundwater extraction is mainly used in the industrial and aquaculture areas, and subsidence in these areas was also observed. As shown in Fig. 11, the subsidence is mainly located in dense industrial zones, where a large number of factories are clustered, such as factories for food, toy, electronics, lighting, furniture, hardware, etc. This shows that subsidence may be induced by groundwater pumping for these industrial uses. For example, subsidence rates between  $-40$  and  $-60$  mm/year are identified near the Liangang Industrial Zone in Jinwan District (Fig. 11a). Fig. 11b is located at Henglan town in Zhongshan city, where

there are many industrial and aquaculture areas with subsidence rates between  $-20$  and  $-30$  mm/year. Fig. 11c is located at the Industrial Zones in Xinhui District, where many factories are distributed and groundwater withdrawal for these factories may cause subsidence during the production cycle. The subsidence rates observed here are between  $-30$  and  $-50$  mm/year, with some areas of about  $-70$  mm/year.

The intensity map of groundwater extraction is collected from Wang et al. (2019b) (Fig. 10c). Groundwater exploitation areas are mainly found in large-scale aquaculture lands (indicated by the letters in Fig. 10a). It can be shown that the distribution of subsidence and groundwater exploitation is mostly similar by contrasting the intensity map of groundwater exploitation (Fig. 10c) with the subsidence map (Fig. 10a). The subsidence rates increase in areas with high groundwater exploitation intensity, such as Doumen and Jinwan districts (Fig. 10a and Fig. 10c). Interestingly, it is worth noting that severe subsidence in Tanzhou town (Fig. 10a) is relatively high, where high groundwater extraction intensity (Fig. 10c) is observed even though the relative thickness of soft soil in this area is not large (Fig. 10b). However, the groundwater exploitation intensity is high (Fig. 10c) in Banfu town (Fig. 10a), but the subsidence is not notable, which may be because of low soft soil thickness (Fig. 10b). The association between groundwater extraction intensity and subsidence under various soft soil thicknesses has been further analyzed to understand the connection between groundwater extraction and subsidence (Table 4). It is found that groundwater extraction can accelerate land subsidence rate in the case of thicker soft soil. Therefore, it is possible to conclude preliminarily that soft soil is the main factor for subsidence in the WPRD, and groundwater extraction is the major triggering factor. This seems to agree with the Gini importance results (Fig. 9) from the RFR.

#### 5.4. Subsidence vs land-use types

Comparing the deformation map (Fig. 4a) with the land-use map (Fig. 7), it can be observed that aquaculture lands are the most prevalent areas for subsidence. Noticeable subsidence is also observed in the urban areas, mainly located in the construction areas of the Xiangzhou district (Fig. 4a), suggesting that there is an obvious correlation between subsidence and land-use types (Fig. 7).

A quantitative analysis is carried out to investigate the relationship between ground subsidence and land-use types. Areas where land-use type remained constant between 2016 and 2021 were selected for analysis to exclude the contribution of land-use change to subsidence.

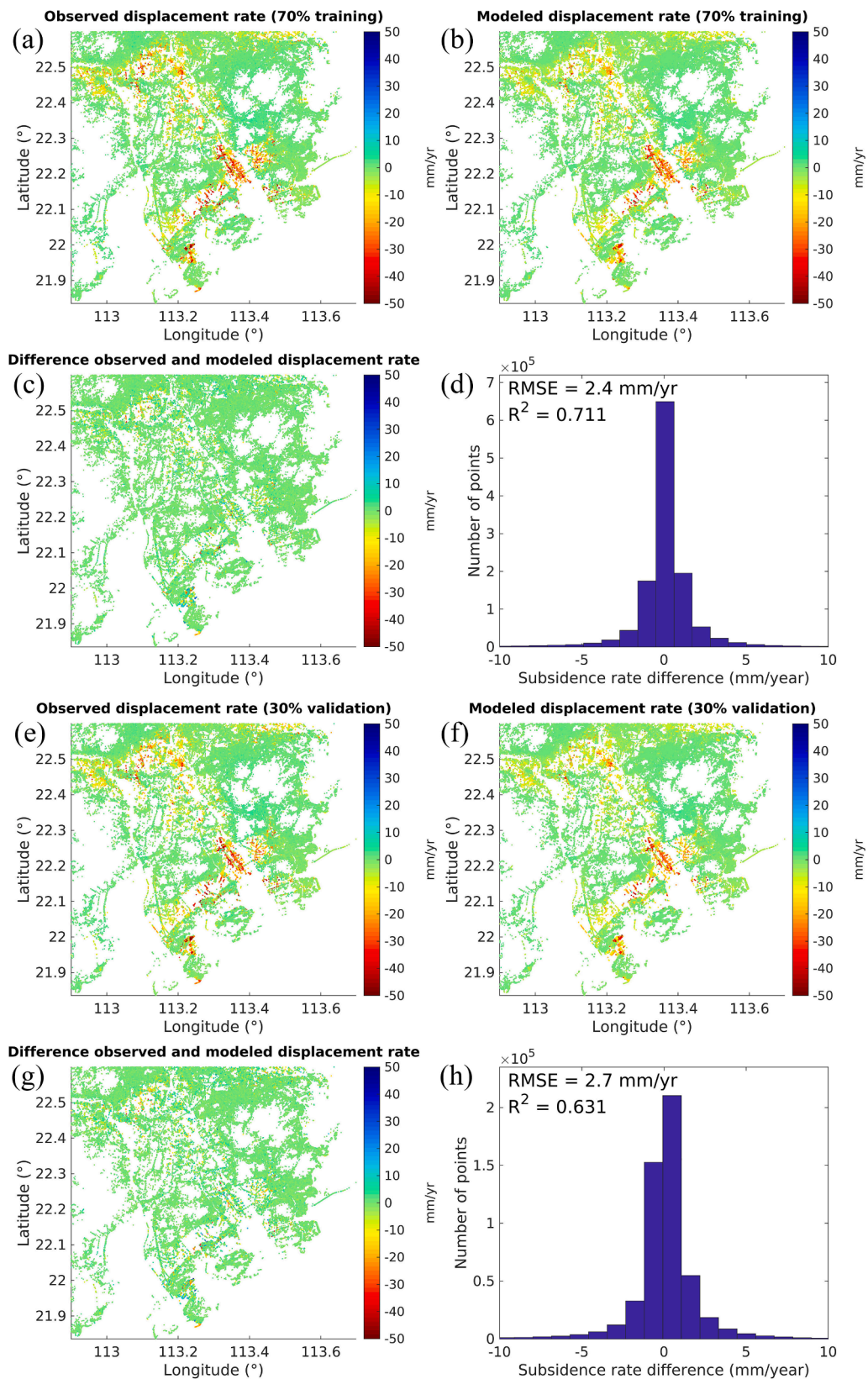


**Fig. 8.** Modeled subsidence results of training and validation dataset; (a) training dataset; (b) modeled subsidence rate of training dataset; (c) subsidence rate difference map between (a) and (b); (d) subsidence rate difference histogram between (a) and (b); (e) validation dataset; (f) modeled subsidence rate of validation dataset; (g) subsidence rate difference between (e) and (f); subsidence rate difference histogram between (e) and (f).

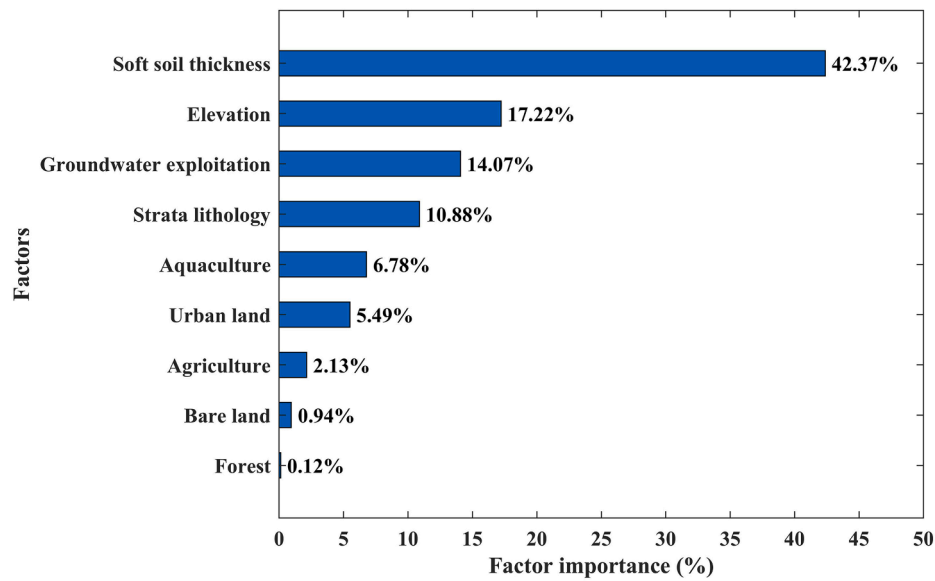


Fig. 9. The proportion of factors influencing the subsidence based on the RFR algorithm.

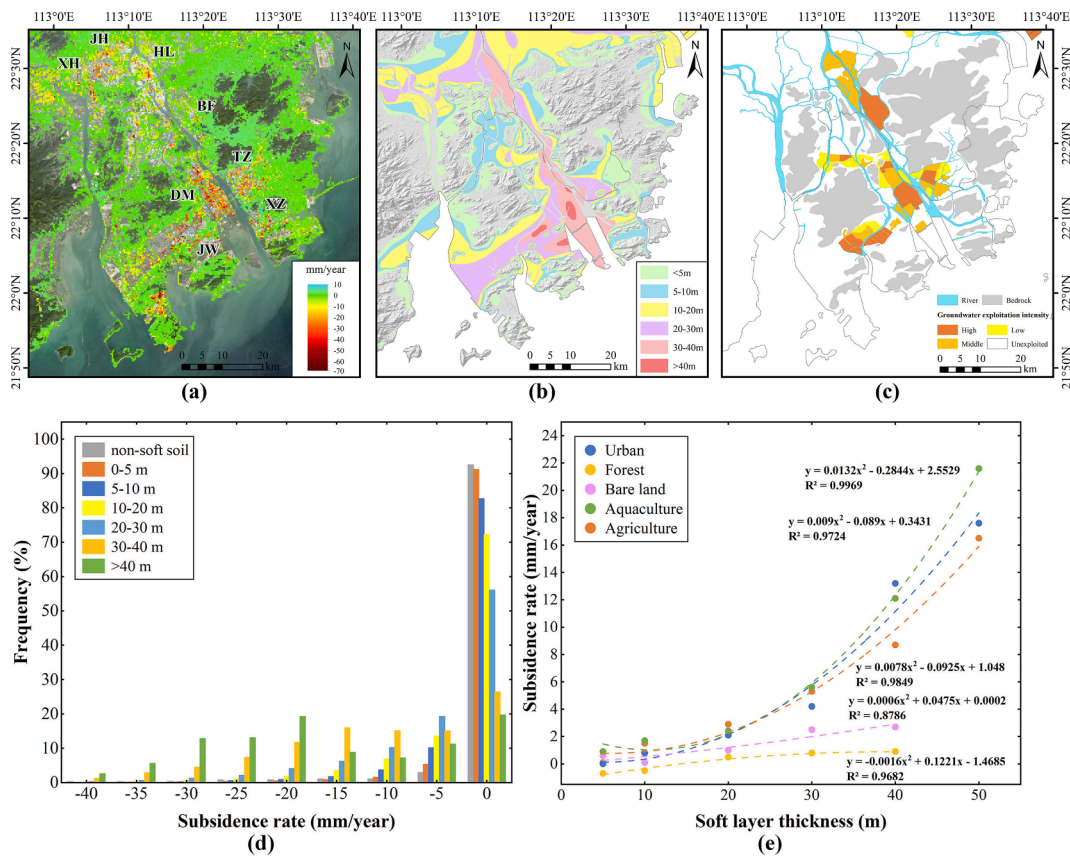


Fig. 10. (a) The subsidence rate map; (b) The distribution map of soft soil thickness; (c) the groundwater exploitation intensity map; (d) the subsidence rate distribution histogram at different soil layer thicknesses and non-soft soil; (e) the correlation between the subsidence rate and soft soil thickness at various land-use types.

The mean subsidence velocities of PS points corresponding to different land-uses for different thicknesses of soft soil were calculated (Table S2). The water bodies and mangroves are not analyzed because of their low coherence properties and small area. It is found that the subsidence rates are proportional to soft soil thickness for all land cover classes. Aquaculture regions experienced the highest subsidence rate, followed by

urban territory and agricultural fields, and then bare land and forests (Fig. 12a). The results reflect a noticeable trend between the impacts of anthropogenic activities on natural systems and the subsidence of various land-use types. In natural and undeveloped areas, such as forests and bare land, the average subsidence rate is relatively low. The small-scale subsidence may be caused by the self-consolidation of soft soil

**Table 3**  
Statistical of PSI measurements for various soft soil thicknesses.

Soft soil thickness (m)	Area (km <sup>2</sup> )	Mean subsidence rate (mm/year)	Standard deviation (mm/year)
<5	547.6	0	2.9
5 ~ 10	402.3	-0.9	4
10 ~ 20	631.8	-2.3	5.6
20 ~ 30	360.5	-4.4	7.7
30 ~ 40	174.3	-11.8	11.5
>40	22.5	-18.2	12.3

(Minderhoud et al., 2018). While regions with more significant anthropogenic influence (such as aquaculture areas, urban land, and agricultural areas) usually have a higher subsidence rate. The cause of subsidence in these areas may be due to the abstraction of groundwater for the cultivation of farmland, aquaculture, and the water demand of urban residents. In addition, the loading on compressible soft soil also causes subsidence in urban territory. Therefore, it can be concluded that more anthropogenic activities cause higher subsidence rates.

5.5. Subsidence vs land-use changes

The deformation rates for land-use conversion that occurred from 2016 to 2021 are compared to investigate the connection between the change in land cover and subsidence. The land-use changes indicate a trend of urban land expansion at the cost of agricultural land. The impact of land-use change on land subsidence under different soft soil

thicknesses was subsequently analyzed (Fig. 12b–f). High land subsidence rate is found in land-use changes with types that demand more groundwater withdrawals and urbanization. For example, aquaculture and urban areas usually experience more significant subsidence because of the increased compaction rate of the aquifer system and surface loading. In the thicker soft soil, land cover types converted into aquaculture have the maximum subsidence rate, followed by urban and agricultural regions. Additionally, the increasing surface displacement rate can be found when the land cover types were converted into urban areas (Fig. 12c), probably due to densely urbanized areas, intensive anthropogenic activities, and surface loading of the compressible deposits by artificial buildings, structures, and infrastructure. The maximum displacement rate occurs in the case of the aquaculture areas

**Table 4**  
Statistical subsidence corresponds to groundwater exploitation intensity in different soft soil thicknesses.

Soft soil thickness (m)	Mean subsidence rates at different groundwater exploitation intensity levels (mm/year)		
	Low	Middle	High
<5	-0.2	-2.0	-0.8
5 ~ 10	-1.7	-2.6	-1.6
10 ~ 20	-3.1	-3.3	-2.2
20 ~ 30	-11.2	-14.3	-5.4
30 ~ 40	-5.9	-12.9	-22.8
>40	-5.1	-21.5	-22.9

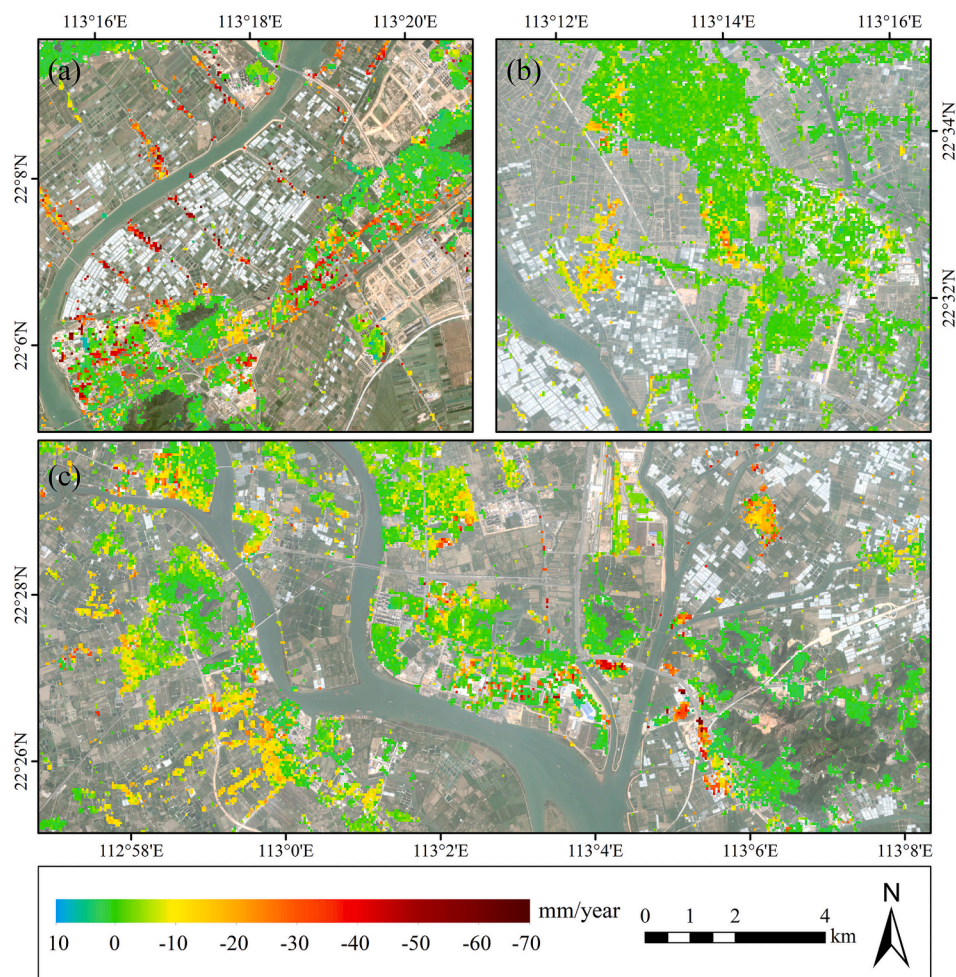


**Fig. 11.** InSAR-derived deformation rate map between 2016 and 2021 in areas where subsidence may be caused by groundwater extraction. (a) Liangang Industrial Zone in Jinwan District, Zhuhai city; (b) Henglan town in Zhongshan city; (c) Industrial Zones in Xinhui District, Jiangmen city.

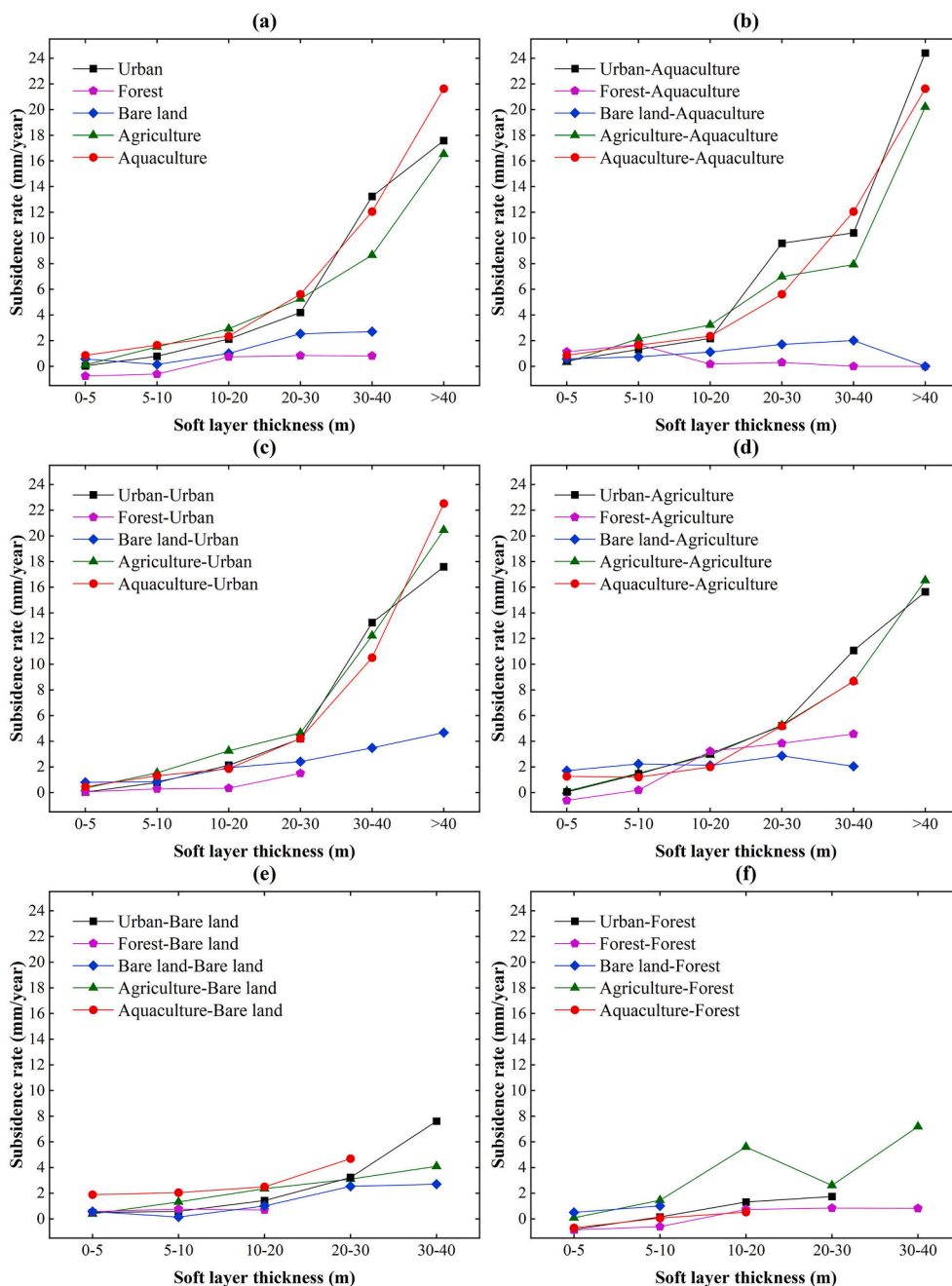


**Fig. 12.** (a) Average subsidence rate of different land-use types at various soft soil thicknesses; (b-f) subsidence rate of different land-use changes between 2016 and 2021 at various soft soil thicknesses.

were converted into the urban territory, followed by the agriculture areas and bare land, with a mean subsidence rate of  $-2.5$  mm/year,  $-1.5$  mm/year, and  $-0.1$  mm/year, respectively. Higher subsidence rate is observed in new urban land than the old urban area. A relatively low subsidence rate was observed in the forest areas (Fig. 12f), probably because forest land is less affected by human activities. Thus, it is less likely to experience land subsidence in this area. It is worth noting that urban land rarely changes into forest in general, and the conversion in this case maybe because of the improvement of ecological environment quality in local areas, but such area is very small (about  $4 \text{ km}^2$ ), as shown in the Land-use transition matrix (Table S1). In addition, misclassification is also unavoidable over the dark shaded areas caused by some vegetation or high buildings, which can easily cause confusion between the two classes. The conversion between urban land and bare land is possibly due to the demolished and rebuilt of the buildings. The

conversion of agricultural land into forest may be the implementation of returning cropland to planted forest, such as the sloping farmland changed into forest (Chen et al., 2021). As for the agricultural land changed into bare land, it is likely the results of social and economic development, where the converted bare land is mainly used for subsequent building construction.

### 5.6. Subsidence vs land reclamation

The blue and red lines shown in Fig. 4a indicate the coastlines of WPRD in 1979 and 2020, respectively. Fig. 4a shows that the most significant subsidence occurs in the reclamation region connecting the Gaolan island. The causes of subsidence in this area were specifically analyzed (Fig. 13). According to the field investigation, there is no significant construction carried out throughout the observation period.

Therefore, the possibility of surface displacement due to building construction is excluded. At the same time, the region is situated at the confluence of the sea and the land, so the soil is mostly muck soil, and most soft soils are unconsolidated (Wang et al., 2019b; Zhang et al., 2021). In addition, Gaolan island was originally a separate island before 2004 and connected to the mainland by 2015, and it underwent large-scale reclamation during this period (Wu et al., 2018; Zhang et al., 2015). So, the long-time consolidation and compaction of the material used for reclamation might have contributed to the subsidence. Reclamation time is also a controlling factor on the stability of the ground structure, with more recently deposited and unconsolidated sediments having higher subsidence rates (Wu et al., 2020; Xu et al., 2016). Fig. 13b and c show the subsidence rates along the profile lines A-A' and B-B' in Fig. 13a. It is found that the ground displacement of the reclamation area before 2005 was relatively low. The subsidence rate of the reclamation area (after 2005) increases rapidly as it becomes further away from the 2005 coastline. This subsidence trend is increasing gradually from land to coast. The explanation for this phenomenon is that the shorter consolidation time of the landfill material may cause greater subsidence (i.e., residual settlement). In summary, geological conditions and reclamation are the dominant causes of severe surface subsidence.

### 5.7. Land subsidence prediction using random forest regression

The predicted subsidence rate map shows a good agreement with the InSAR results with similar spatial patterns (Fig. 8). This suggests that most of the spatial variability in the study area observed by InSAR is associated with the factors used in subsidence prediction. Fig. 9 shows that the most dominating factor affecting the land subsidence in this region is the thickness of soft soil, accounting for 42.37 %, followed by elevation and groundwater exploitation, accounting for 17.22 % and 14.07 %, respectively. For the impacts of land-use classes on subsidence, the highest score was associated with aquacultural land (6.78 %), followed by urban land (5.49 %), and agricultural land (2.13 %). Again, aquaculture and agriculture are closely associated with groundwater extraction, both of which have a considerable impact on land displacement (Higgins et al., 2013; Yuen et al., 2021). The load of building land on the soft soil can also lead to land subsidence (Cui et al., 2015), while bare land and forest areas, appear to have negligible effects on subsidence (<1 %). This indicates they contributed little to increased accuracy in the model. Therefore, more land-use types may not need to be

considered when analyzing the relationship between subsidence and land-use types in this area.

In addition, to further confirm the model's applicability in this area. The dataset was divided: 30 % of samples are used for training with the remaining 70 % being utilized for validation. The model was trained with fewer observations to predict more unknown regions to assess the model's dependability. The results are shown in Fig. 14. The predicted subsidence rate map with a resolution of 30 m. The RMSE between the InSAR measured and the predicted subsidence rate is 2.9 mm/year ( $R^2 = 0.579$ ). This combined approach of InSAR and RFR shows the potential to expand the applicability of InSAR with short-wavelength SAR data over the decorrelated areas (e.g., vegetated regions). The land historical data can be used together with the InSAR-measured observations to train the subsidence model for ground settlement prediction. It is also found that combining the land-use historical data to predict subsidence rates, in addition to the land-use during the acquisition period, greatly improves prediction results. Therefore, land-use time series data with a time span as long as possible is preferred for subsidence rate prediction. The use of land-use history maps to estimate subsidence for the entire region provides a possible way for data enhancement in decoherent regions and some areas due to the lack of data for direct subsidence monitoring. For example, some subsidence signals were not detected by InSAR due to decorrelation, but were revealed from the prediction results. Since the relationship between multiple influencing factors and subsidence is considered, which may provide better results and more accurate interpretability than conventional methods that only consider location factors (such as spatial interpolation). Three areas were selected for discussion, as shown in Fig. 15. Fig. 15a is located in Hengqin District, and there are a lot of engineering construction activities that led to decorrelation in the InSAR-derived subsidence results. It is observed that the subsidence is relatively serious with the subsidence rate of about 40–60 mm/year. It can be seen that the predicted result revealed more subsidence signals (Fig. 15d), and the subsidence in the construction area can cause large social and economic losses, so more attention should be paid to the subsidence status in this area. The predicted subsidence signals can be used to complement InSAR for the limitation of the spatial coverage of subsidence monitoring and provide more subsidence information. Moreover, in some regions with few PS points, such as aquaculture and agricultural land, where the human engineering activities are relatively little. However, heavy groundwater extraction activities, which may also lead to subsidence, are expected. As shown in Fig. 15b and c, the

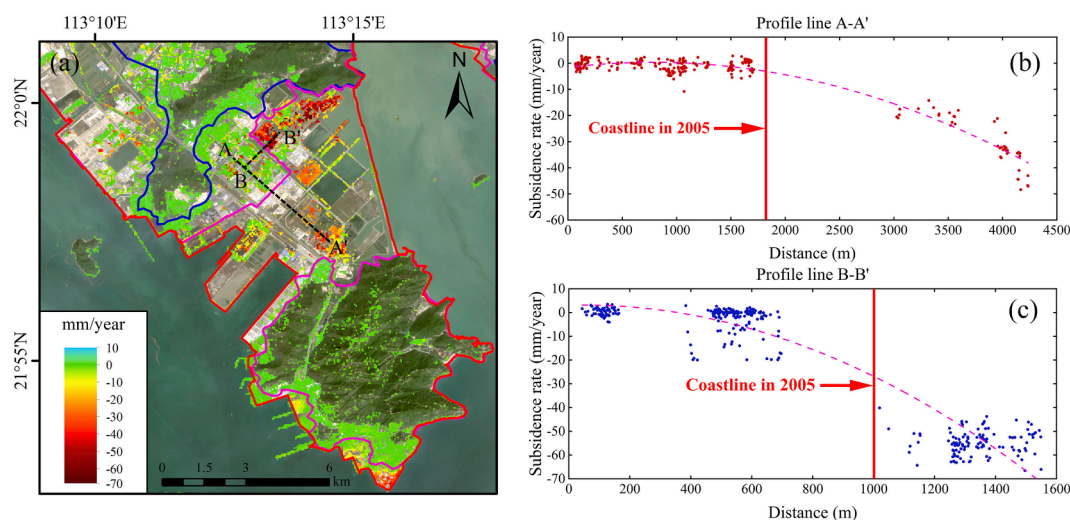


**Fig. 13.** (a) Average subsidence rate in the land reclamation area of Gaolan island. The blue, purple, and red lines represent the coastline in 1979, 2005, and 2020. The black dotted lines denote the subsidence profile A-A' and B-B' in this reclamation area. The subsidence rate along the profile lines (b) A-A' and (c) B-B'. (For interpretation of the references to colour in this figure legend, the reader is referred to the web version of this article.)

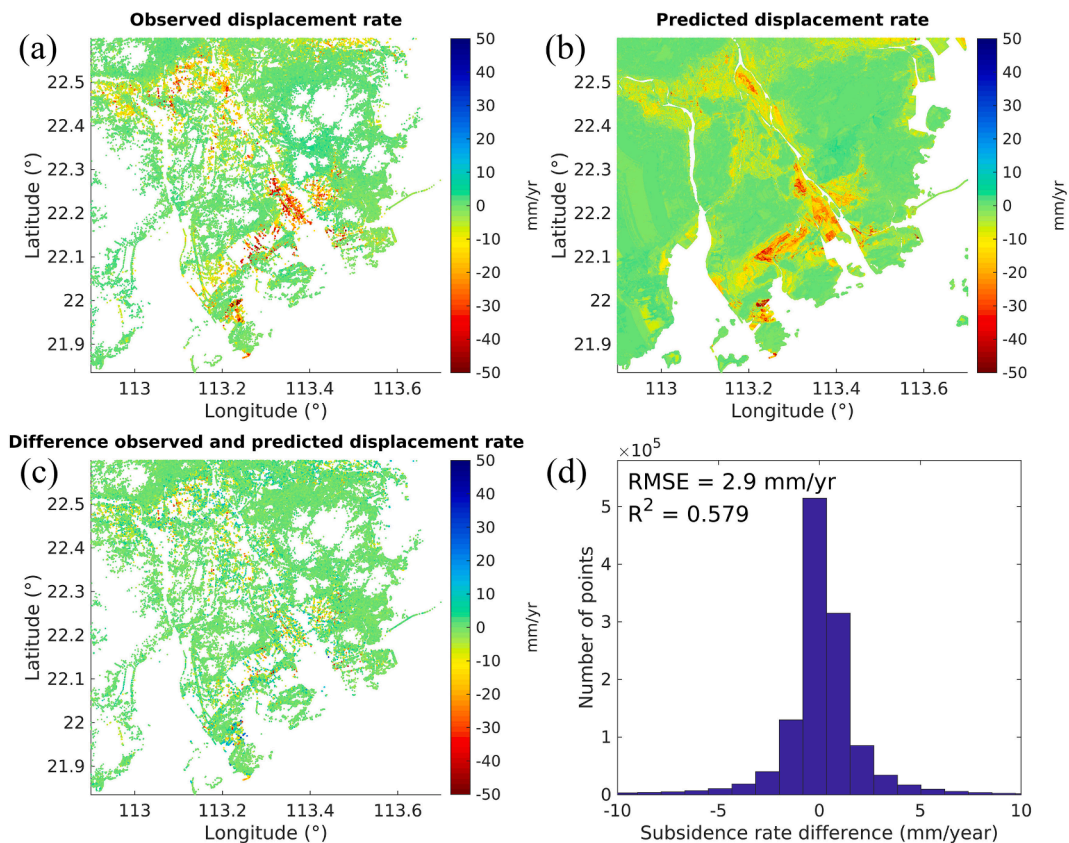


Fig. 14. (a) InSAR-measured subsidence rate map; (b) the predicted subsidence rate map derived from the RFR model (with 30% of the measurements used as training samples); (c) subsidence rate difference map between observations and predictions; (d) subsidence rate difference histogram between observations and predictions.

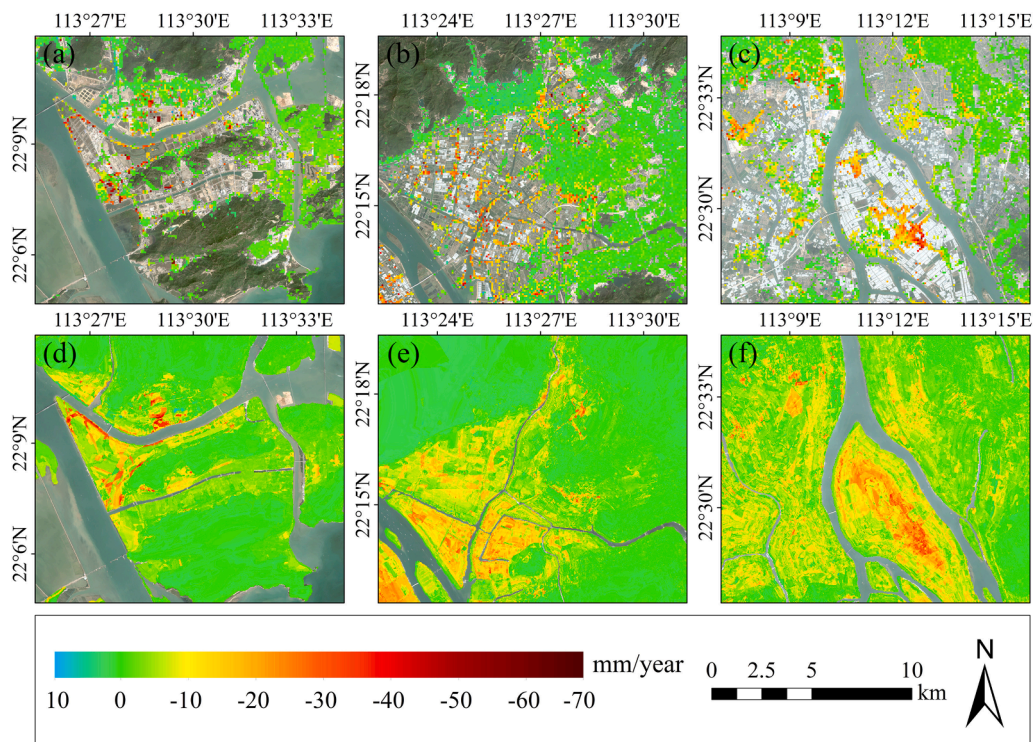


Fig. 15. (a-c) InSAR results; (d-f) the subsidence prediction results corresponding to (a-c).

aquaculture and agricultural land are widely distributed, and the subsidence is relatively serious. Fig. 15b shows that there are few PS points detected and the subsidence rate is about 30–50 mm/year. Fig. 15c is located in Xinhui District and the subsidence rate in this area is about 20–40 mm/year. It can be seen from Fig. 10b and c that the thickness of soft soil in this area is relatively thick (20–40 m), and the groundwater exploitation is relatively intensive, both of which may be the main reasons for the serious subsidence. The predicted results in Fig. 15e and f show more subsidence signals. However, the predicted results may be slightly biased due to the coarser resolution of input data for model construction, but these subsidence factors are obvious and the modeled results (Fig. 8) showed that it hardly affects the overall spatial pattern of subsidence.

In addition to the spatial pattern, it is possible for the subsidence model to provide temporal trends of subsidence. Some studies have shown that groundwater exploitation and land use have a time-lag effect on land subsidence (Chen et al., 2019; Minderhoud et al., 2018). Therefore, based on the subsidence model constructed in this study, it may be possible to use existing groundwater and land use data to predict the temporal trend of subsidence in the future.

### 5.8. Subsidence management and prevention

According to InSAR-derived subsidence rates and the importance assessment of subsidence influence factors in the WPRD, urban construction and subsidence prevention work in this area should mainly be carried out from the following aspects. Firstly, large-scale engineering construction activities should be avoided as much as possible in areas with thick soft soil, and pre-pressure treatment of soft soil foundation should be prioritised before engineering construction, or reliable engineering measures should be taken to mitigate the engineering quality problems caused by soft soil subsidence. Moreover, subsidence monitoring in the soft soil area should be strengthened to monitor the trends of subsidence in real-time, so as to provide a scientific basis for the management and decision-making of relevant departments and institutions. Secondly, in order to reduce the exploitation of groundwater in the study area, the long-term monitoring of groundwater level should be strengthened in the aquaculture area, and the exploitation of groundwater should be strictly controlled. Finally, this study shows an obvious correlation between land cover types and subsidence, which can be used to guide sustainable land use in the WPRD. For example, reducing the conversion of other land cover types to buildings and aquaculture land, and promoting conversion to land cover types less susceptible to subsidence. In addition, spatial subsidence assessment can also help to provide a comprehensive understanding of the subsidence status and formulate policies and plans for subsidence mitigation measures.

## 6. Conclusion

Based on the time-series InSAR techniques, sixty-seven Sentinel-1 images are applied to monitor the land subsidence of the WPRD between 2016 and 2021. The overall subsidence rates of the WPRD range from –70 to 10 mm/year. Three subsidence bowls were identified in this region, located on the Gaolan island of Zhuhai city, the junction of Zhuhai and Zhongshan, and the junction of Zhongshan and Jiangmen respectively. Obvious correlation between subsidence and Quaternary soft soil has been observed. It is observed that the thickness of the soft soil is directly proportional to the subsidence rate. This reveals that soft soil consolidation is the primary contributing factor to surface displacement. Land subsidence is also found to be greatly affected by the intensity of groundwater exploitation, and groundwater exploitation can accelerate land settlement.

The comparison between the subsidence rate and land-use data suggests that the most significant subsidence was observed in the aquaculture, followed by urban land and agricultural land, and finally,

bare land and forests. For all of the land-use types that were transformed into urban land, the maximum subsidence rate was observed with aquaculture to urban, followed by the agricultural land to urban and bare land to urban. Moreover, severe subsidence is found in the reclamation area. The effect of consolidation and residual subsidence is expected to be stronger in the new reclamation land, and hence larger subsidence may be expected. At last, the RFR method with an RMSE of 2.7 mm/year reveals the potential to estimate land subsidence by soft soil thickness, groundwater exploitation, land-use history, elevation, and strata lithology. The results show that the predicted displacement velocities are relatively consistent with the surface deformation derived by InSAR. The soft soil thickness has the strongest relationship with land subsidence. The land-use classes that affect the subsidence are mainly aquaculture, urban land, and agricultural land.

In general, a variety of causes influence land subsidence in the WPRD. The distribution of soft soil is expected to be the main subsidence factor, while human activities can trigger and accelerate land subsidence. Subsidence in the WPRD is expected to continue if no measures are taken to mitigate it. Hence the findings could serve as a guide for urban construction and land-use planning in the WPRD.

### CRediT authorship contribution statement

**Ziyue Liu:** Methodology, Software, Formal analysis, Investigation, Writing – original draft, Visualization, Validation. **Alex Hay-Man Ng:** Conceptualization, Methodology, Software, Investigation, Resources, Writing – review & editing, Supervision. **Hua Wang:** Conceptualization, Methodology, Supervision, Data curation, Writing – review & editing. **Jiawei Chen:** Investigation, Data curation. **Zheyuan Du:** Writing – review & editing, Investigation, Validation. **Linlin Ge:** Writing – review & editing, Resources, Supervision.

### Declaration of Competing Interest

The authors declare that they have no known competing financial interests or personal relationships that could have appeared to influence the work reported in this paper.

### Acknowledgments

The authors thank ESA for providing the Sentinel-1A/B data. This research was funded by the Program for Guangdong Introducing Innovative and Entrepreneurial Teams (2019ZT08L213), National Natural Science Foundation of China (Grant no. 42274016/D0402), Natural Science Foundation of Guangdong Province (grant number 2021A1515011483).

### Data availability statement

The InSAR and the land-use data are available on request from the authors. The ground survey and soil layer data are not available due to legal restrictions.

### Appendix A. Supplementary material

Supplementary data to this article can be found online at <https://doi.org/10.1016/j.jag.2023.103228>.

### References

- Bakr, M., 2015. Influence of groundwater management on land subsidence in Deltas. *Water Resour. Manag.* 29, 1541–1555.
- Breiman, L., 2001. Random Forests. *Mach. Learn.* 45, 5–32.
- Chen, B., Gong, H., Lei, K., Li, J., Zhou, C., Gao, M., Guan, H., Lv, W., 2019. Land subsidence lagging quantification in the main exploration aquifer layers in Beijing plain, China. *Int. J. Appl. Earth Obs. Geoinf.* 75, 54–67.

- Chen, X., Li, F., Li, X., Hu, Y., Hu, P., 2021. Quantifying the compound factors of forest land changes in the pearl river delta. *China. Remote Sensing* 13, 1911.
- Chen, F., Lin, H., Zhang, Y., Lu, Z., 2012. Ground subsidence geo-hazards induced by rapid urbanization: implications from InSAR observation and geological analysis. *Nat. Hazards Earth Syst. Sci.* 12, 935–942.
- Colesanti, C., Ferretti, A., Novali, F., Prati, C., Rocca, F., 2003. SAR monitoring of progressive and seasonal ground deformation using the permanent scatterers technique. *IEEE Trans. Geosci. Remote Sens.* 41, 1685–1701.
- Cui, Z.-D., Yang, J.-Q., Yuan, L., 2015. Land subsidence caused by the interaction of high-rise buildings in soft soil areas. *Nat. Hazards* 79, 1199–1217.
- Du, Y., Feng, G., Liu, L., Fu, H., Peng, X., Wen, D., 2020. Understanding Land Subsidence Along the Coastal Areas of Guangdong, China, by Analyzing Multi-Track MTInSAR Data. *Remote Sens. (Basel)* 12, 299.
- Du, Z.Y., Ge, L.L., Ng, A.H.M., Lian, X.G., Zhu, Q.G.Z., Horgan, F.G., Zhang, Q., 2021. Analysis of the impact of the South-to-North water diversion project on water balance and land subsidence in Beijing, China between 2007 and 2020. *J. Hydrol.* 603 (B), 126990.
- Ferretti, A., Prati, C., Rocca, F., 2001. Permanent scatterers in SAR interferometry. *IEEE Trans. Geosci. Remote Sens.* 39, 8–20.
- Foga, S., Scaramuzza, P.L., Guo, S., Zhu, Z., Dilley Jr, R.D., Beckmann, T., Schmidt, G.L., Dwyer, J.L., Hughes, M.J., Laue, B., 2017. Cloud detection algorithm comparison and validation for operational Landsat data products. *Remote Sens. Environ.* 194, 379–390.
- Galloway, D.L., Erkens, G., Kuniansky, E.L., Rowland, J.C., 2016. Preface: Land subsidence processes. *Hydrogeol. J.* 24, 547–550.
- Higgins, S., Overeem, I., Tanaka, A., Syvitski, J.P.M., 2013. Land subsidence at aquaculture facilities in the Yellow River delta, China. *Geophys. Res. Lett.* 40, 3898–3902.
- Kuang, J., Ng, A.-H.-M., Ge, L., 2022. Displacement Characterization and Spatial-Temporal Evolution of the 2020 Aniangzhai Landslide in Danba County Using Time-Series InSAR and Multi-Temporal Optical Dataset. *Remote Sens. (Basel)* 14, 68.
- Lai, B., Jiang, J., Liu, J., 2021. Analysis of ground subsidence monitoring in zhuhai city based on PS-InSAR Technology. *Res. Environ. Eng.* 35.
- Li, Z., Dang, X., Cai, M., Zhao, J., Yu, L., Li, X., 2021. Subsidence monitoring and analysis of Zhuhai based on PSInSAR technology. *J. Nat. Disasters* 30, 38–46.
- Li, G., Feng, G., Xiong, Z., Liu, Q., Xie, R., Zhu, X., Luo, S., Du, Y., 2020. Surface deformation evolution in the Pearl River Delta between 2006 and 2011 derived from the ALOS1/PALSAR images. *Earth Planets Space* 72, 1–14.
- Loupe, G., Wehenkel, L., Sutera, A., Geurts, P., 2013. Understanding variable importances in forests of randomized trees. *Advances in neural information processing systems* 26.
- Lu, Y., 2006. Report on 1/250,000 Ecological Environment Geological Survey Results of Pearl River Delta Economic Zone. Guangdong Geological Survey Institute.
- Ma, P., Wang, W., Zhang, B., Wang, J., Shi, G., Huang, G., Chen, F., Jiang, L., Lin, H., 2019. Remotely sensing large- and small-scale ground subsidence: a case study of the Guangdong-Hong Kong-Macao Greater Bay Area of China. *Remote Sens. Environ.* 232, 111282.
- Minderhoud, P., Coumou, L., Erban, L., Middelkoop, H., Stouthamer, E., Addink, E., 2018. The relation between land use and subsidence in the Vietnamese Mekong delta. *Sci. Total Environ.* 634, 715–726.
- Ng, A.-H.-M., Ge, L., Li, X., Abidin, H.Z., Andreas, H., Zhang, K., 2012a. Mapping land subsidence in Jakarta, Indonesia using persistent scatterer interferometry (PSI) technique with ALOS PALSAR. *Int. J. Appl. Earth Obs. Geoinf.* 18, 232–242.
- Ng, A.-H.-M., Ge, L., Li, X., Zhang, K., 2012b. Monitoring ground deformation in Beijing, China with persistent scatterer SAR interferometry. *J. Geod.* 86, 375–392.
- Ng, A.-H.-M., Wang, H., Dai, Y., Pagli, C., Chen, W., Ge, L., Du, Z., Zhang, K., 2018. InSAR Reveals Land Deformation at Guangzhou and Foshan, China between 2011 and 2017 with COSMO-SkyMed Data. *Remote Sens. (Basel)* 10.
- Rabus, B., Eineder, M., Roth, A., Bamler, R., 2003. The shuttle radar topography mission—a new class of digital elevation models acquired by spaceborne radar. *ISPRS J. Photogramm. Remote Sens.* 57, 241–262.
- Rosen, P.A., Gurrrola, E., Sacco, G.F., Zebker, H., 2012. The InSAR scientific computing environment, EUSAR 2012; 9th European Conference on Synthetic Aperture Radar, pp. 730–733.
- Umarhadi, D.A., Widyatmanti, W., Kumar, P., Yunus, A.P., Khedher, K.M., Kharrazi, A., Avtar, R., 2022. Tropical peat subsidence rates are related to decadal LULC changes: insights from InSAR analysis. *Sci. Total Environ.* 816.
- Wang, H., Wright, T.J., Yu, Y., Lin, H., Jiang, L., Li, C., Qiu, G., 2012. InSAR reveals coastal subsidence in the Pearl River Delta, China. *Geophys. J. Int.* 191, 1119–1128.
- Wang, H., Wright, T.J., Liu-Zeng, J., Peng, L., 2019a. Strain rate distribution in south-central tibet from two decades of InSAR and GPS. *Geophys. Res. Lett.* 46, 5170–5179.
- Wang, S., Yan, X., Jie, J., Yang, T., Wu, J., Wang, H., 2019b. Analysis on factors affecting ground settlement in plain area of Pearl River Delta. *The Chinese J. Geol. Hazard and Control* 30.
- Wu, Z., Milliman, J.D., Zhao, D., Cao, Z., Zhou, J., Zhou, C., 2018. Geomorphologic changes in the lower Pearl River Delta, 1850–2015, largely due to human activity. *Geomorphology* 314, 42–54.
- Wu, S., Yang, Z., Ding, X., Zhang, B., Zhang, L., Lu, Z., 2020. Two decades of settlement of Hong Kong International Airport measured with multi-temporal InSAR. *Remote Sens. Environ.* 248.
- Xu X. Liu, J. Zhang, S. Li, R. Yan, C. Wu, S. 2018. China's Multi-period Land Use Land Cover Remote Sensing Monitoring Data set (CNLUCC). Resource and Environment Data Cloud Platform: Beijing, China.
- Xu, B., Feng, G., Li, Z., Wang, Q., Wang, C., Xie, R., 2016. Coastal subsidence monitoring associated with land reclamation using the point target based SBAS-InSAR Method: A Case Study of Shenzhen, China. *Remote Sensing* 8, 652.
- Yang, Z.F., Li, Z.W., Zhu, J.J., Hu, J., Wang, Y.J., Chen, G.L., 2016. InSAR-based model parameter estimation of probability integral method and its application for predicting mining-induced horizontal and vertical displacements. *IEEE Trans. Geosci. Remote Sens.* 54, 4818–4832.
- Yuen, K.W., Tang Thi, H., Vu Duong, Q., Switzer, A.D., Teng, P., Lee, J.S.H., 2021. Interacting effects of land-use change and natural hazards on rice agriculture in the Mekong and Red River deltas in Vietnam. *Nat. Hazards Earth Syst. Sci.* 21, 1473–1493.
- Zhang, J., 1997. Tentative research on hydrogeological and engineering geological features of Zhuhai city. *J. Geol. Hazards Environ. Preservation* 7–13.
- Zhang, Y., Huang, H., Liu, Y., Bi, H., Zhang, Z., Wang, K., Yan, L., 2021. Impacts of soft soil compaction and groundwater extraction on subsidence in the Yellow River Delta. *Mar. Georesour. Geotechnol.* 39, 1497–1504.
- Zhang, W., Xu, Y., Hoitink, A., Sassi, M., Zheng, J., Chen, X., Zhang, C., 2015. Morphological change in the Pearl River Delta, China. *Mar. Geol.* 363, 202–219.
- Zhu, Z., Vuik, V., Visser, P.J., Soens, T., van Wesenbeeck, B., van de Koppel, J., Jonkman, S.N., Temmerman, S., Bouma, T.J., 2020. Historic storms and the hidden value of coastal wetlands for nature-based flood defence. *Nat. Sustainability* 3, 853–862.